ACSNANO
www.acsnano.org
ARTICLE

Magnetic Nanoliposomes as *in Situ* Microbubble Bombers for Multimodality Image-Guided Cancer Theranostics

Yang Liu,[†,§] Fang Yang,[*,†,§] Chuxiao Yuan,[†] Mingxi Li,[†] Tuantuan Wang,[†] Bo Chen,[†] Juan Jin,[†] Peng Zhao,[†] Jiayi Tong,[‡] Shouhua Luo,[†] and Ning Gu[*,†]

[†]State Key Laboratory of Bioelectronics, Jiangsu Key Laboratory for Biomaterials and Devices, School of Biological Science and Medical Engineering, Southeast University, Nanjing 210096, People's Republic of China

[‡]Institute of Cardiology, Southeast University, Nanjing 210009, People's Republic of China

Supporting Information

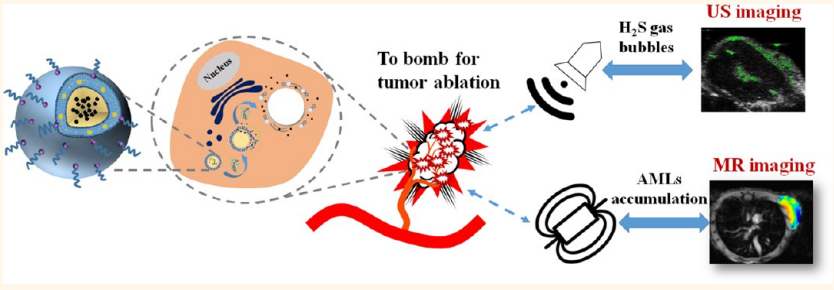

ABSTRACT: **Nanosized drug delivery systems have offered promising approaches for cancer theranostics. However, few are effective to simultaneously maximize tumor-specific uptake, imaging, and therapy in a single nanoplatform. Here, we report a simple yet stimuli-responsive anethole dithiolethione (ADT)-loaded magnetic nanoliposome (AML) delivery system, which consists of ADT, hydrogen sulfide (H_2S) pro-drug, doped in the lipid bilayer, and superparamagnetic nanoparticles encapsulated inside. HepG2 cells could be effectively bombed after 6 h co-incubation with AMLs. For *in vivo* applications, after preferentially targeting the tumor tissue when spatiotemporally navigated by an external magnetic field, the nanoscaled AMLs can intratumorally convert to microsized H_2S bubbles. This dynamic process can be monitored by magnetic resonance and ultrasound dual modal imaging. Importantly, the intratumoral generated H_2S bubbles imaged by real-time ultrasound imaging first can bomb to ablate the tumor tissue when exposed to higher acoustic intensity; then as gasotransmitters, intratumoral generated high-concentration H_2S molecules can diffuse into the inner tumor regions to further have a synergetic antitumor effect. After 7-day follow-up observation, AMLs with magnetic field treatments have indicated extremely significantly higher inhibitions of tumor growth. Therefore, such elaborately designed intratumoral conversion of nanostructures to microstructures has exhibited an improved anticancer efficacy, which may be promising for multimodal image-guided accurate cancer therapy.**

KEYWORDS: *magnetic nanoliposomes, hydrogen sulfide, in situ microbubbles, ultrasound theranostics, multimodal imaging*

Effective cancer theranostics have recently become topics of intensive research interest. Nanosized drug delivery systems are one of the appealing approaches because of their highly adjustable surface to carry both therapeutic and imaging agents.[1,2] In recent years, numerous chemical- or physical-based stimuli-responsive formulations or devices for controlled drug release have been developed.[3] For example, stimuli-sensitive "smart" nanocarriers specifically responding to the tumor microenvironment (low pH,[4] altered redox potential,[5] hypoxia,[6] hyperthermia,[7] *etc.*) and/or external stimuli (magnetic field,[8] light,[9] ultrasound,[10] *etc.*) have been designed to enhance the tumor targeting and antitumor effect due to the precise regulation of intracellular delivery fate. Various kinds of elaborate nanosized carriers such as liposomes,[11] micelles,[12] noble metal nanoparticles,[13] metal oxide nanoparticles,[14] and metal−organic nanostructures[15] indeed have demonstrated enhanced therapeutic effects in comparison with conventional anticancer carriers due to their size-dependent targeting, transvascular permeability, and intratumoral diffusion properties.[16,17] However, the physiological barriers imposed by the abnormal tumor vasculature and the dense collagen matrix have prevented nanocarriers from being

Received: October 10, 2016
Accepted: January 3, 2017
Published: January 3, 2017

DOI: 10.1021/acsnano.6b06815
ACS Nano 2017, 11, 1509−1519

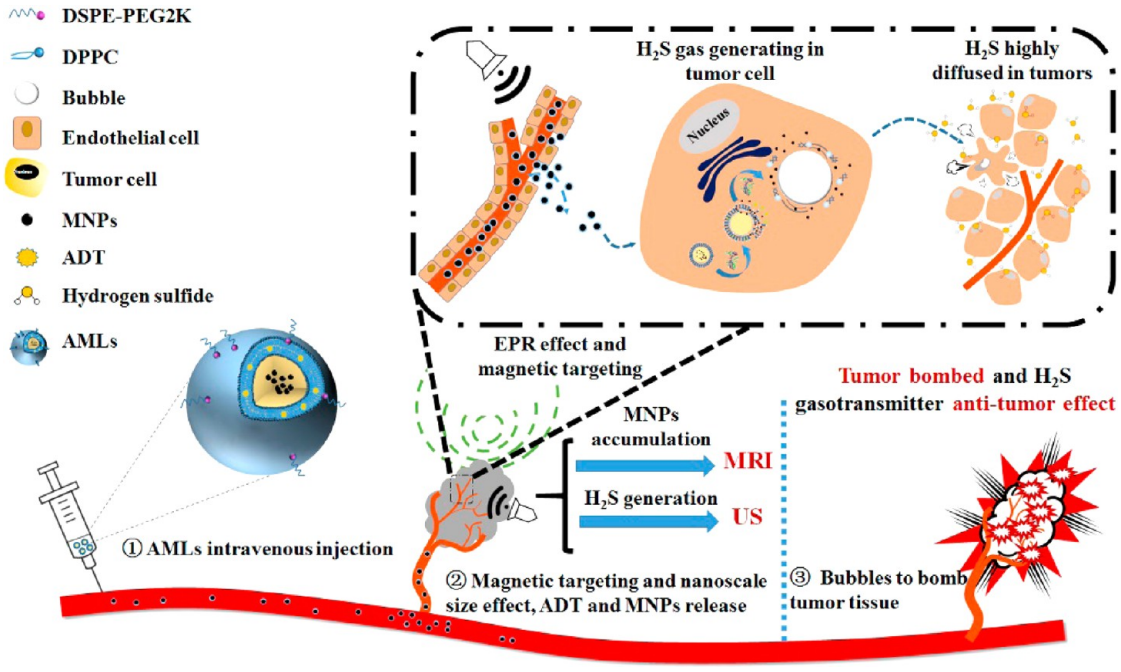

Figure 1. Concepts and schematics of AMLs and their nano to micro conversion for US/MR dual modal imaging and the spatiotemporal-bombed combination tumor accurate therapy.

delivered to unperfused deep tumor regions,[18] resulting in weakening the effectiveness of cancer therapeutics. Nanocarriers are frequently surface modified with targeting ligands to improve targeting, internalization, and retention in tumors.[19,20] Nevertheless, binding to cell surface receptors restricts nanocarriers from residing on the vessel wall surface,[21,22] which actually prevents them entering the inner regions of the tumor. Besides, due to the relatively complex and disorganized morphological and physiological structure of tumors, nanocarriers themselves also display high possibility of washout back to the blood circulation even by using the current combined physical and chemical approaches.[23,24] Therefore, a nanotheranostics platform and paradigm aimed at the improvement of nanocarrier accumulation and distribution in the tumor's poorly accessible regions is still challenging.

Here, we present the idea of intratumoral conversion of nanostructures to microstructures as excellent diagnosis modality and potential therapeutic effects for imaging-monitored accurate tumor ablation. The simple yet stimuli-responsive nanostructures are small superparamagnetic nanoparticles (core diameter about 7 nm) that are encapsulated in the aqueous core of the liposomes (about 200 nm diameter) with hydrophobic anethole ditholethione (ADT) doped in the phospholipid shell. The anethole dithiolethione (ADT)-loaded magnetic nanoliposomes (AMLs) with originally a ~200 nm diameter preferentially extravasate from the leaky regions of the tumor vasculature, resulting in perfusion in the tumor microvascular and the interstitial matrix by spatiotemporally stimulating the external magnetic field.[25] It has been well-documented that tumor neovasculature is typically abnormal in form and architecture; this phenomenon is referred to as the enhanced permeability and retention (EPR) effect.[26] Then, the specific intratumoral accumulation and distribution of AMLs can be dynamically monitored by magnetic resonance (MR) imaging. At the same time, with the release of ADT molecules (organic hydrogen sulfide (H_2S) donors)[27] in the tumor matrix, large numbers of microsized H_2S bubbles can be continuously generated *via* an enzymatic trigger.[28] As shown in Figure 1, such a nano- to microsize change enables AMLs to be localized within the tumor microenvironment, preventing their washout. Simultaneously, real-time ultrasound (US) imaging can be used to determine the dynamic H_2S microbubble production process. Moreover, guided by microbubble- enhanced US imaging, the H_2S microbubbles acting like an intratumoral bomber could explode to ablate the local tumor tissue when applying a higher acoustic intensity for bubble cavitation.[29] The burst of microbubbles and the diffusion of intratumoral high-concentration H_2S molecules[30] in the deep tumor region may synergistically enhance the antitumor effect. Therefore, the unique feature of *in situ* microbubble generation ensures that AMLs could serve as significant contrast enhancement in MR and US dual modal imaging. As a synergistic "Trojan Horse"-like bomber, H_2S gasotransmitter antitumor agents further strengthen tumor ablation efficiency.

RESULTS AND DISCUSSION

Design, Fabrication, and Characterization of AMLs. The bare liposomes without loading superparamagnetic nanoparticles (MNPs) and ADT, ADT-encapsulated liposomes (ALs), and ADT-encapsulated magnetic liposomes (AMLs) were prepared by hydration and a membrane-extrusive method. The AMLs were fabricated with ADT formulated within the lipid bilayer and γ-Fe_2O_3 magnetic nanoparticles encapsulated in the core of the liposome structure. This process is shown in Figure 2a. Dynamic light scattering (DLS) measurement showed that the size of the formed bare liposomes was 165.8 ± 1.98 nm with a polydispersity index (PDI) of 0.13 (Figure 2c). In a separate reaction, superparamagnetic nanoparticles were synthesized following a previously published protocol,[31] resulting in MNPs with a nearly uniform size of 7 nm measured by transmission electron microscopy (TEM) (Figure 2a). The MNPs were then diluted in phosphate-buffered saline (PBS) solution mixed with a dried lipid film to create a lipid emulsion.

DOI: 10.1021/acsnano.6b06815
ACS Nano 2017, 11, 1509–1519

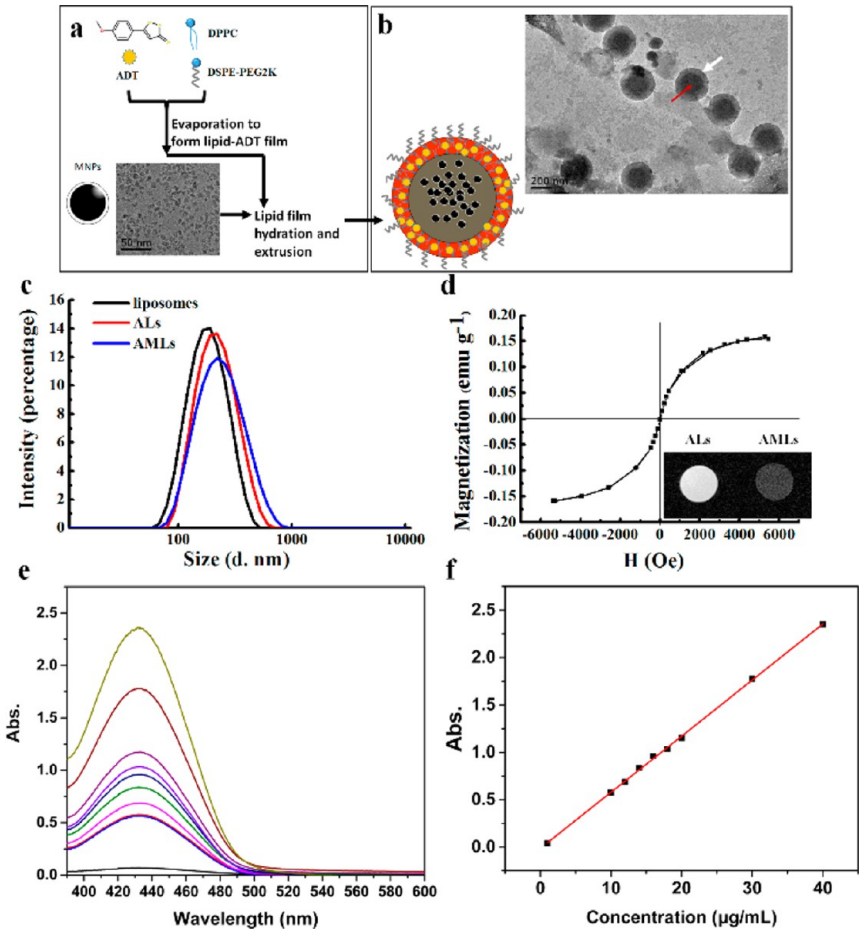

Figure 2. Fabrication and characterization of AMLs. (a) Diagram of AMLs fabricated by loading both ADT and MNPs. (b) Schematics and representative TEM images of AMLs. The white arrow indicates the ADT inserted in the lipid membrane. Red arrows demonstrate the existence of MNPs in the core of the liposomes. (c) Size distribution of liposomes, ALs, and AMLs, respectively. (d) VSM curve of AMLs at room temperature. Insets show the *in vitro* MRI of AL and AML (86.1 μg/mL iron concentration) solutions. (e) Ultraviolet absorption spectra of ADT doped in liposomes. (f) Absorbance units of ADT at different loading concentrations and linear fitting curve.

The excess MNPs and ADT in the emulsion was removed by Sephadex G50 gel-permeation columns. DLS data showed that the size of the ALs and AMLs was 200.4 ± 3.41 nm with a PDI of 0.15 and 211.1 ± 4.64 nm with a PDI of 0.19, respectively (Figure 2c). The morphology and structure of the three formed liposomes were further imaged by TEM. As shown in Figure 2b, the presence of MNPs trapped and dispersed in the core of the nanostructure was confirmed by the visible high electron density area in the liposomes. Meanwhile, the clear shell membrane in the magnified TEM image also indirectly indicated the presence of ADT in the shell membrane of AMLs.

As a H_2S gas organic pro-drug, hydrophobic ADT was selected to dope the lipid bilayer. To further confirm the insertion of ADT in the liposome membranes, the synthesized liposome sample was verified by ultraviolet−visible (UV−vis) spectroscopy. Figure 2e shows the representative ultraviolet absorption spectra of the ADT liposomes in the range of 400−600 nm at different loading concentrations with an absorption wavelength of 432 nm. According to the electron transition mechanism, the ADT was identified as doping the liposome shell. Then we further investigated ADT loading capacities in the liposomes with increasing concentrations ranging from 0 to 40 μg/mL. As shown in Figure 2f, when the loading concentration increased, the absorption intensity increased and showed a good linear relationship between absorbance and concentration. The optimized encapsulation efficiency of ADT in the liposomes was 49.6 ± 3.4% with a concentration of 14.9 μg/mL. On the basis of the standard iron concentration curve in Figure S1, the encapsulated MNPs' concentration in the liposomes was measured to be 172.1 μg/mL.

The magnetic performance of the AMLs was investigated at room temperature using a vibrating sample magnetometer (VSM) (model 7407, Lake Shore Cryotronics, Inc., USA). Figure 2d shows the magnetic hysteresis curves of the AMLs. No remanent magnetization was observed in the curve, indicating that the superparamagnetic behavior of AMLs was preserved. As controls, no magnetic hysteresis curves were obtained for ALs and liposomes. The inset pictures in Figure 2d indicate the best contrast of MRI of AMLs (86.1 μg/mL iron concentration) in solution to change the T_2* signal. T_2* values collected from liposomes, ALs, and AMLs were 340.01 ± 82.64, 388.13 ± 83.11, and 12.85 ± 2.19 ms, respectively. The 96.2% decrease in T_2* value of the AMLs compared to blank liposomes indicated that γ-Fe_2O_3 MNPs have been efficiently encapsulated into the liposomes, which in turn endows the AMLs with excellent MR imaging ability. Simultaneously, AMLs are able to spatially and temporally be controlled by fine-tuning the area where and the time when the external magnetic fields are applied.

DOI: 10.1021/acsnano.6b06815
ACS Nano 2017, 11, 1509−1519

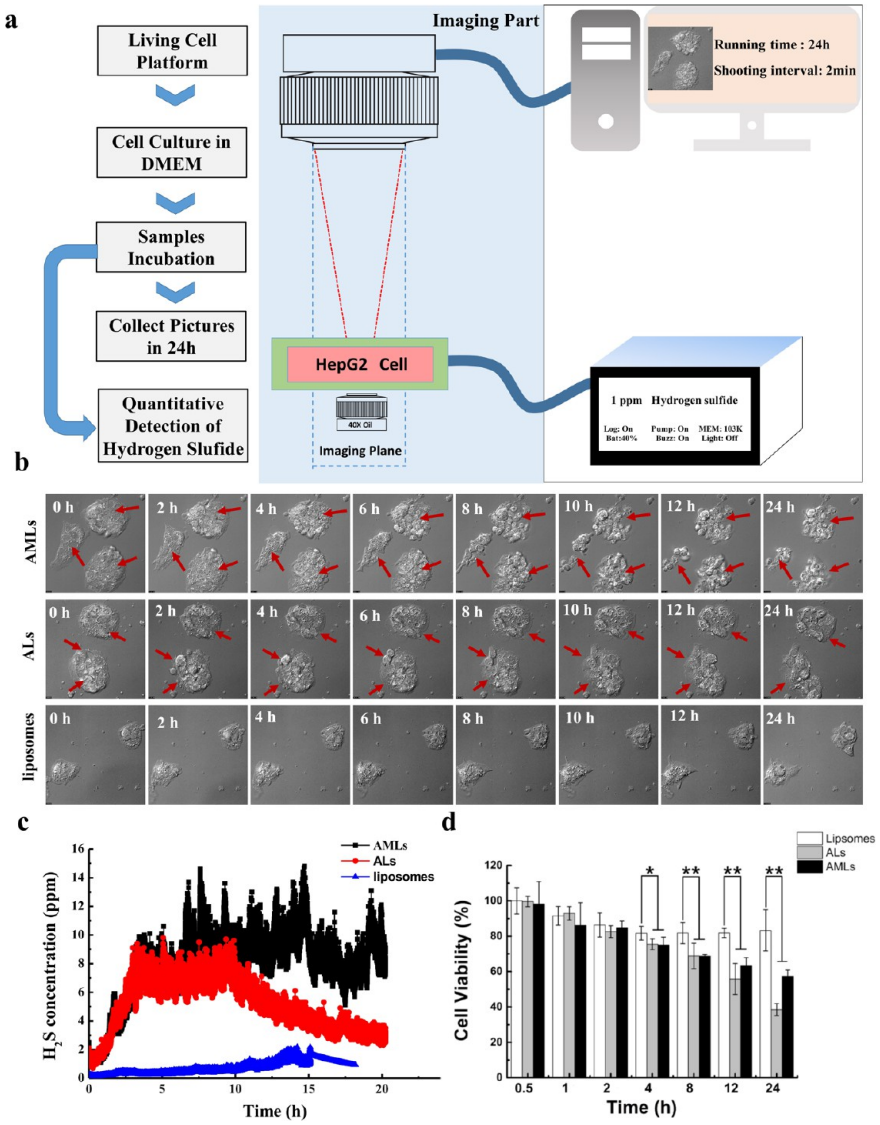

Figure 3. Live cell optical system for observation of cell morphology change and cell viability after incubation with liposomes, ALs, and AMLs. For each sample, a time gradient was acquired. (a) Experimental setup for the real-time optical imaging and H_2S quantitative measurement. (b) Cellular morphology change and intracellular bubble generation captured at time points of 0, 2, 4, 6, 8, 10, 12, and 24 h for AMLs, ALs, and liposomes, respectively. Red arrows indicate the bubble generation and significant cell membrane disruption. Scale bar: 50 μm. (c) Real-time quantitative detection of intracellular H_2S generation. (d) Viability of HepG2 cells when incubated with samples at different time points. The statistical significance is indicated by $^{**}p < 0.01$ and $^{*}p < 0.05$.

Real-Time H_2S Mapping in Tumor Cells. It has been reported that ADT molecules can generate H_2S gas triggered by cystathionine-β synthase (CBS) and cystathionine-γ-lyase (CSE).[32] These two major enzymes have been demonstrated in most tissues including tumor tissue.[33,34] Here, the generation of H_2S gas at the cell level from AMLs was first investigated. Endocytosis of HepG2 cells by three types of samples including liposomes, ALs, and AMLs was monitored by a real-time live cell optical imaging system (IX71, Olympus Co. Ltd., Japan). The H_2S bubbles generated from the intracellular AMLs' release of ADT were visualized and captured by optical microscopy, and at the same time, the quantitative H_2S concentration was measured by a H_2S gas detector, which is schematically shown in Figure 3a. The optical microscopic images of a HepG2 cell at typical incubation time points of 0, 2, 4, 6, 8, 10, 12, and 24 h were captured from the dynamics acquisition of the H_2S microbubble production process (Video S1, Supporting Information), as shown in Figure 3b. The results demonstrate that HepG2 cells incubated with blank liposomes showed intact morphology within 24 h. However, when incubated with AMLs, a change in cellular morphology and even cell rupture was observed. At the very beginning of adding AMLs (0 h), it was found that the cells naturally adhered to the dish bottom with smooth morphology. After about 2.5 h of incubation, the edge of the cells began to become irregular and some intracellular bubble-like bumps appeared (red arrows in Figure 3b). After 6 h of incubation, the cells were disrupted and detached from the dish bottom. Prussian blue staining of the MNPs in Figure S2 (Supporting Information) further demonstrated that the intracellular H_2S production resulted from HepG2 cell uptake of AMLs. After that, the cells were bombed into irregular debris with the successive increase of the bubble amount. This significant cellular morphology change and disruption phenomenon

DOI: 10.1021/acsnano.6b06815
ACS Nano 2017, 11, 1509−1519

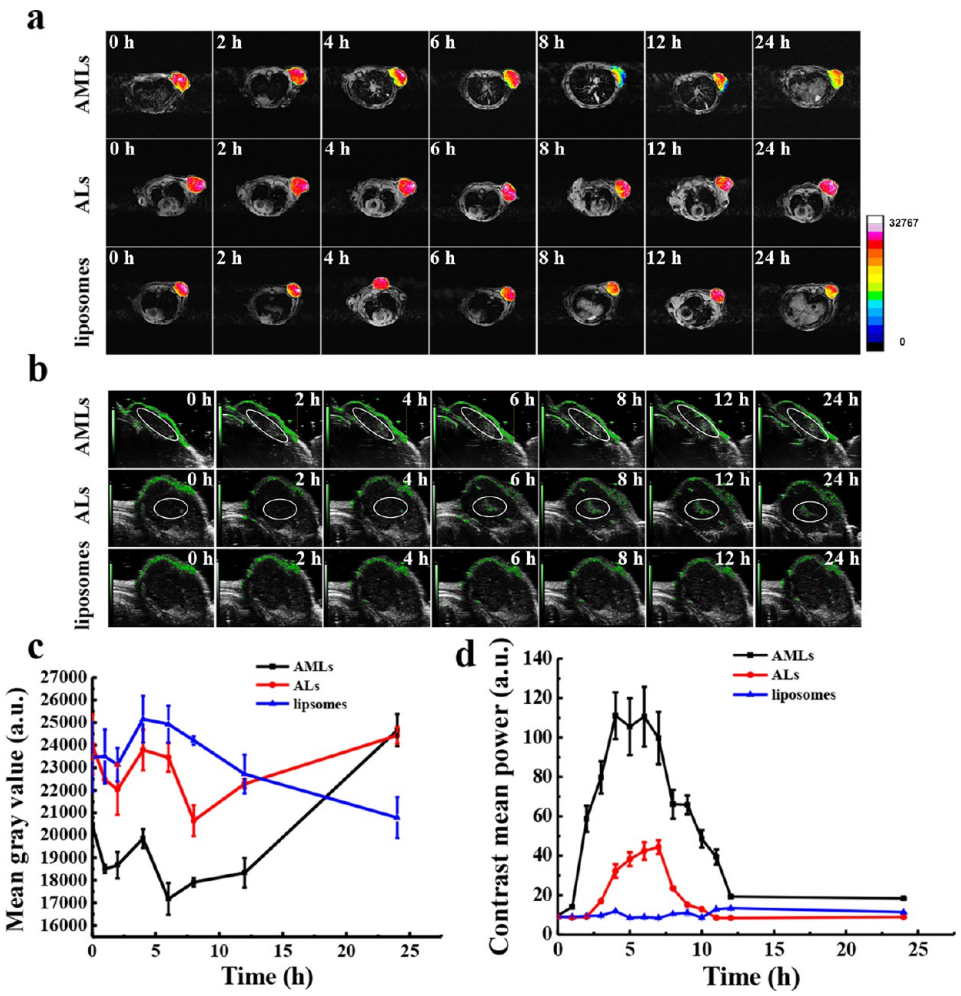

Figure 4. Time-dependent *in vivo* MR and US imaging of tumors after intravenous injection of AMLs, ALs, and liposomes in a HepG2-bearing mouse model. (a) *In vivo* T_2 MR images before (0 h) and after AML, AL, and liposome injection (2, 4, 6, 8, 12, 24 h). (b) *In vivo* US images of mouse tumor before (0 h) and after AML, AL, and liposome injection (2, 4, 6, 8, 12, 24 h). Average mean gray value of the T_2 MRI signal (c) and mean contrast enhanced grayscale of US imaging (d) time courses. The average mean gray time course shows the different change tendencies after injection of AMLs, ALs, and liposomes.

clearly indicate that AMLs could generate H_2S bubbles to induce HepG2 cell death. Compared to AMLs, ALs showed a similar morphology change, which may be because H_2S production mainly relies on intracellular ADT release.

Simultaneously, in order to monitor the amount of intracellular H_2S molecules, gas detector (IQ-1000, International Sensor Technology, CA, USA) with a H_2S gas sensor (International Sensor Technology) was used to detect H_2S dynamic production. Figure 3c shows the quantification of H_2S acquired from a HepG2 cell solution when incubated with liposomes, ALs, and AMLs, respectively. Without ADT loading, no H_2S concentration was measured. Nevertheless, in the presence of ADT in the liposomes for both ALs and AMLs, after internalization with HepG2 cells, with the release of ADT into the cell, H_2S gas production was triggered. For AMLs and ALs, the total amount of H_2S produced was 6.56×10^{-3} and 9.29×10^{-3} μmol, reaching a maximum after about 4 h of incubation. There was no significant difference between AMLs and ALs, which further demonstrated that the H_2S production mainly came from the ADT concentration in the liposomes.

Correspondingly, to quantitatively examine the cell necrosis during the incubation, HepG2 cells were collected after 0, 0.5, 1, 2, 4, 8, 12, and 24 h of incubation and the cell viability was quantitatively assessed by the CCK-8 assay. The result in Figure 3d shows that the cell viability of both ALs and AMLs decreased after 4 h of incubation. After 12 h of incubation, about 50% of the cells died in both the AL and AML treatment groups. According to the observed dynamic cell morphology change and the confirmation of intracellular H_2S production, two factors may contribute to the death of HepG2 cells: (1) After the endocytosis of nanosized AMLs, a massive amount of microsized H_2S gas bubbles, originating from the sustained H_2S gas generation due to the ADT enzymatic trigger, were produced inside the cell. Such intracellular "nano- to microsize" expansion can behave like bubble bombers to explode and physically destroy the cells. (2) It has been reported that there may be a delicate balance induced by exogenous H_2S administration between cancer cell proliferation and death depending on the concentration and releasing time. Generally, relatively high concentrations of H_2S or a relatively low level of H_2S over a relatively long time period may selectively inhibit cancer cell proliferation.[35,36] As shown in Figure S3a,b (Supporting Information), the lower ADT concentration (1.49, 2.98 μg/mL) indicated no cytotoxicity or low cytotoxicity (cell viability was above 80%) on HepG2. Figure 3c indicates the continually relatively long time release frame

DOI: 10.1021/acsnano.6b06815
ACS Nano 2017, 11, 1509−1519

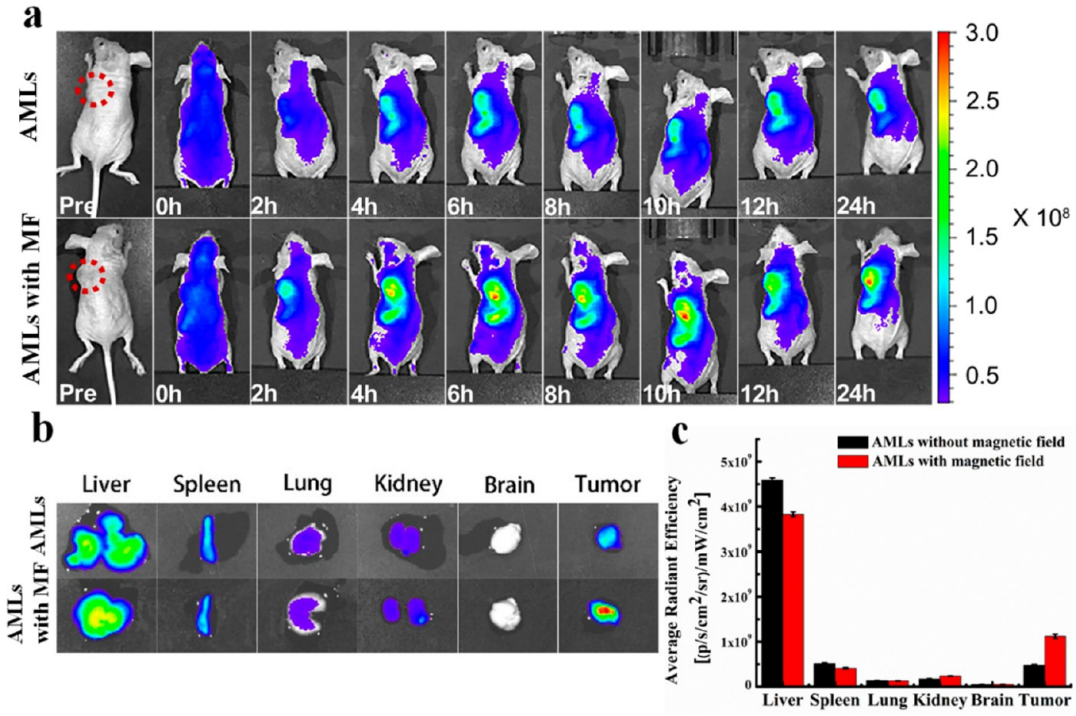

Figure 5. ***In vivo*** **NIR-fluorescence imaging of AMLs in tumor-bearing mice. (a) Time course of DiR-fluorescence images of a mouse bearing a subcutaneous HepG2 xenograft on its back injected with DiR-coupled AMLs with and without external magnetic field treatment over time (0, 2, 4, 6, 8, 10, 12, 24 h). The look-up tables presented have units of radiant efficiency (p/s/cm²/sr)/(μW/cm²). (b)** ***Ex vivo*** **NIR-fluorescence imaging of excised organs (liver, spleen, lung, kidney, brain, and tumor). (c) Bar graph showing the integrated intensities of DiR fluorescence in select organs excised from mice injected with DiR-coupled AMLs with and without external magnetic field treatment.**

(0−16 h) and high H_2S dose (6.56×10^{-3} and 9.29×10^{-3} μmol for ALs and AMLs) during the co-incubation. Thereby, the continued H_2S release triggered by ADT- catalyzed reaction after endocytosis may further enhance the optimal anticancer effects. As a control, the L02 cells, normal hepatocytes, were co-incubated with liposomes, ALs, and AMLs with the highest ADT concentrations (5.96 μg/mL). The result in Figure S3c (Supporting Information) of the CCK-8 assay indicates that there is no significant cytotoxicity on L02 cells after incubation for 0, 0.5, 1, 2, 4, 8, 12, and 24 h.

In Vivo **Enhanced Tumor Internalization with US/MRI Dual Mode Imaging Monitoring.** To establish the feasibility of tumor magnetic targeting by AMLs *in vivo*, a proof of concept study was performed on three groups of BALB/C nude HepG2-bearing mice with the tumor volume of each mouse reaching approximately 100 mm^3. AMLs were injected intravenously to anesthetized nude HepG2 xenograft-bearing mice; the other two groups of mice injected with ALs and blank liposomes were treated as control groups. According to the protocol of the experimental design shown in Figure S4 (Supporting Information), on injection, the external static magnetic field was located right outside the tumor tissue. High-resolution MRI (7 T) was performed pre- and postinjection of blank liposomes, ALs, and AMLs, and the tumor MRI data were collected at equivalent time intervals (0, 2, 4, 6, 8, 12, and 24 h). As shown in Figure 4a, the blank liposome and AL solution groups did not give any tumor T_2* signal decrease after being injected intravenously. It is clear that for the AML group, the mean gray value of tumor area decreased about 22% 6 h after injection. When a 16-color layer was added by ImageJ (NIH, USA), the MR images clearly demonstrated that the injected AMLs diffused to the whole tumor regions at 6 h postinjection. The mean gray intensity value of T_2* images in the AML group shown in Figure 4c was almost 2 times lower 6 h after injection than the AL group. These findings demonstrate the efficiency of AMLs to infiltrate the tumor with an enhanced accumulation when a magnet is applied to target the AMLs, which can be readily detected by MRI.

On the basis of the excellent results of the gas-bubble-generating performance in cells, we further explored the US imaging capabilities *in vivo* after intravenous injection of AMLs. The real-time property of US imaging authentically verified whether ADT could be enzyme-sensitive to produce H_2S microbubbles for US tumor diagnosis. Microbubble-enhanced US imaging was performed on three different groups (liposomes, ALs, and AMLs) as MRI experiments. Figure 4b shows typical US tumor imaging, which indicates that enhanced US imaging can be observed in the inner region of the tumor. The echo intensity value of US in the AMLs group reached a maximum 4 h after injection, which was almost 3.4 times higher than the AL group (Figure 4d). The significant difference between ALs and AMLs could be attributed to the strong magnetic field induction of the AMLs to target the tumor. When exposed to an external magnetic field, the MNPs can guide AMLs through the blood vessels by the magnetic force, causing the AMLs to passively target the tumor site in addition to the EPR effect of the liposomes. Once the AMLs were intratumorally accumulated, the released ADT was then enzyme-catalyzed to generate H_2S bubbles. The *in situ* generated bubbles act as US contrast agents to sensitize the US imaging signal. Thus, the microbubble-enhanced US imaging could be utilized to monitor the whole intratumoral H_2S dynamic production process (from generation, destruction, and diffusion). Since the conversion of AMLs into H_2S bubbles

DOI: 10.1021/acsnano.6b06815
ACS Nano 2017, 11, 1509−1519

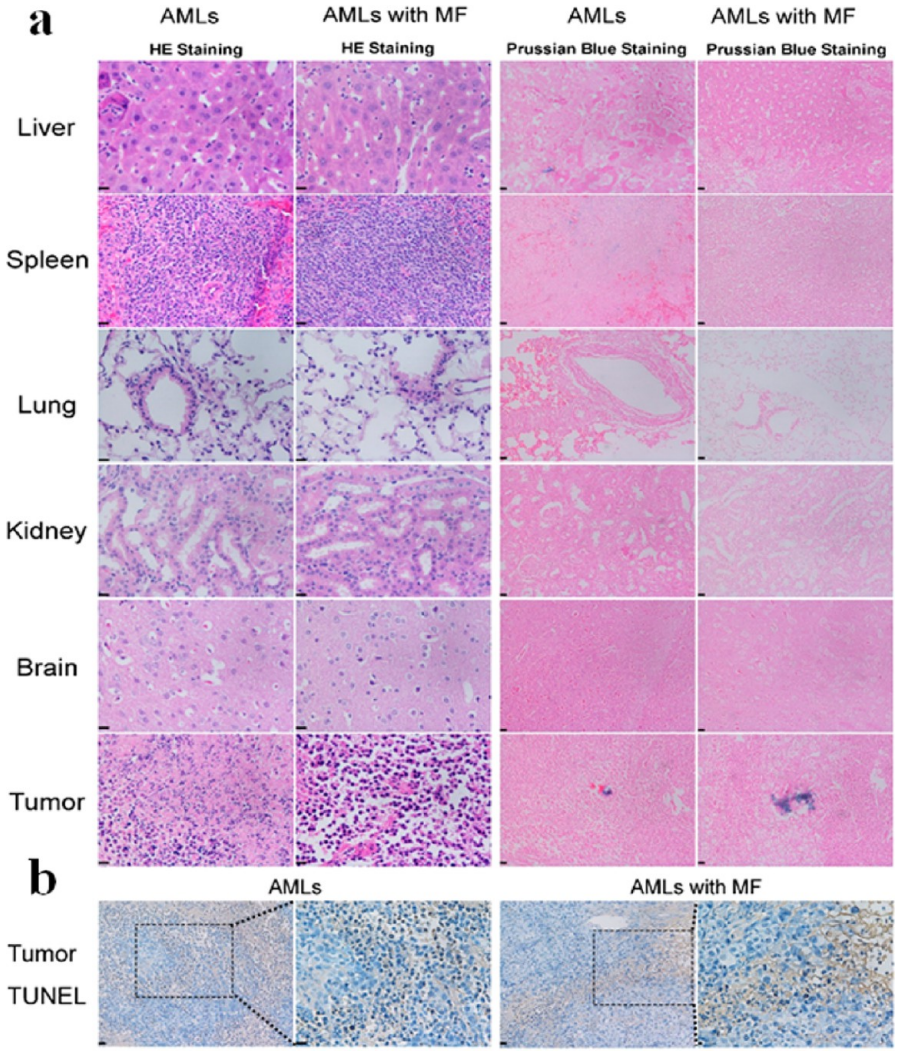

Figure 6. Histological analysis of excised tumors and major organs (liver, spleen, lung, kidney, and brain) after AMLs with and without magnetic field (MF) treatment. (a) Hematoxylin/eosin (HE) staining and Prussian blue staining are shown. (b) TUNEL assay for tumors. All scale bars are 20 μm.

can be monitored by US imaging in real time, spatiotemporally controlled tumor therapy induced by bubble cavitation under the higher acoustic intensity can be obtained.

A major limitation of current nanocarrier cancer therapies is the inability of nanostructure therapeutics to penetrate throughout the entire tumor mass.[37] This inhomogeneous distribution of carrier therapeutics within the tumor has been linked to treatment failure and incomplete elimination. Normally, the total flux of material toward the tumor can be interpreted as in eq 1:[38]

$$J_{\text{Total}} = PA(C_v - C_i) + L_pA[(P_v - P_i) - \sigma(\pi_v - \pi_i)](1 - \sigma_F)C_v + \text{Black Box} \quad (1)$$

where $PA(C_v - C_i)$ is the diffusive component originating from the Brownian motion of colloids. $L_pA[(P_v - P_i) - \sigma(\pi_v - \pi_i)]$ represents the flux of fluid and drag of the colloid by the fluid (σ_F) and the colloid concentration in the vascular compartment (C_v). The "black box" indicates the complex interaction with intracellular and/or extracellular targets within the tumor environment. It is well-known that liposomes provide better pharmacokinetics and biodistribution of theranostic agents than many other carriers due to high agent-loading efficiency, high stability in biological environments, controllable release kinetics, and biocompatibility.[39] In this study, the PEG modification in the liposomal formulation can result in prolonged circulation in the blood and enhanced passive EPR accumulation in the tumor. Then tumoral uptake of liposomes can be further improved due to the magnetically responsive (Figure 1e) moiety of γ-Fe_2O_3 in the AMLs under the exposure of an external magnetic field. Each AML is subjected to a drag force from the blood vessel and to a magnetophoretic force from the magnetic field, resulting in enhanced liposome permeability and distribution within the tumor. Finally, with the release of ADT, the H_2S bubbles can be generated and diffuse in the tumor. With the increased production of H_2S bubbles, not only can the decreased perfusing pressure (P_v) improve the transvascular convective movement, leading to faster rates of nanoliposome delivery, but also the intratumoral nano- to microsize change could promote intratumoral penetration of AMLs and prevent AMLs from being washed out.

***In Vivo* Distribution Evaluation of AMLs.** Because of the superior *in vivo* US and MR imaging performance based on MNP accumulation and H_2S generation in the tumor, we further investigated the biodistribution of AMLs with and

DOI: 10.1021/acsnano.6b06815
ACS Nano 2017, 11, 1509–1519

without an external magnetic field. A near-infrared (NIR) fluorescence *in vivo* imaging system (IVIS Spectrum, Caliper Life Science, USA) was used to image and analyze (Living Image 5.0 software) the distributions of AMLs with and without an external magnetic field. Labeled by a DiR (1,1′-dioctadecyl-3,3,3′,3′-tetramethylindotricarbocyanine iodide) cell membrane fluorescent dye, AMLs were injected into the tail veins of HepG2 tumor-bearing mice (n = 5 per group), and whole-body DiR-fluorescence images recorded over time (0, 2, 4, 6, 8, 10, 12, and 24 h). AMLs were found throughout the body with and without an external magnetic field during the first 4 h, as evidenced by the strong and uniform DiR fluorescence in representative mice shown in Figure 5a. The accumulation of AMLs in a tumor was evident about 6 h after AML injection. The targeting of AMLs to tumor was further enhanced under exposure to an external magnetic field. The major organ distribution of AMLs was evaluated by recording DiR fluorescence from the organs excised from mice injected with AMLs with and without external magnetic field treatment (Figure 5b). The area-normalized DiR-fluorescence signals from excised tumors were 2.34 times higher for DiR-coupled AMLs with an external magnetic field compared to without an external magnetic field ($(1.12 \pm 0.05) \times 10^9$ *vs* $(4.78 \pm 0.21) \times 10^8$ $(p/s/cm^2/sr)/(\mu W/cm^2)$, respectively). DiR fluorescence was also evident in the excised livers of mice injected with AMLs with and without magnetic field exposure ($(3.83 \pm 0.52) \times 10^9$ *vs* $(4.59 \pm 0.47) \times 10^9$ $(p/s/cm^2/sr)/(\mu W/cm^2)$, respectively). AML accumulation in these organs was expected, as liposomes are known to be cleared by Kupfer cells. The effectiveness of AMLs in targeting tumors was further evaluated by calculating the ratio of DiR fluorescence among excised organs (tumor, liver, spleen, and kidney). The ratios for the tumor/liver, tumor/spleen, and tumor/kidney were consistently higher for AMLs with magnetic field exposure compared to those without magnetic field treatment and calculated as 0.29 *vs* 0.10, 2.72 *vs* 0.93, and 6.40 *vs* 1.16, respectively, with all p-values being less than 0.05.

Therapeutic Efficacy Evaluation for Tumors. Finally, the therapeutic efficiency of the AMLs in the tumor-bearing nude mouse model was evaluated. The therapeutic protocol was that when microbubble-enhanced US imaging reached a maximum 6 h after injection of AMLs. The therapeutic US intensity of the burst model in a VisualSonics Vevo 2100 high-resolution microimaging system (VisualSonics Vevo 2100, Canada) was used to disrupt the H_2S bubbles (Figure S4, Supporting Information). After US treatment, the mouse was euthanized by a lethal dose of pentobarbital. The tumors were harvested and fixed in 10% neutral buffered formalin, processed, and paraffin embedded for the histopathological analysis. Tumor-bearing mice were also treated with either bare liposomes or ALs (no MNPs) as controls. Histological analysis of hematoxylin and eosin (HE) staining and the TUNEL assay for tissue sections retrieved from the tumor further supported the therapeutic efficacy of AMLs (Figure 6). No obvious histopathological abnormalities or lesions were observed in the main organs (liver, spleen, lung, kidney, and brain) for AMLs with and without magnetic field exposure, implying low acute toxicity or little risk from AMLs. HE staining of the tumor indicated the enhanced antitumor effect following magnetic field treatment, possibly because gas bubbles destroyed the cellular membrane, then inside components were excreted from necrotic cells, leading to the deep blue cell nucleus separating away from the pink cytoplasm. Besides, in order to confirm that the localized MR signal drop may be attributed to the accumulation of MNPs donated by AMLs, the results were compared with histological sections of tumors after Prussian blue staining. Accumulations of MNPs were found in the liver and tumor using Prussian blue and nuclear fast red double staining (Figure 6a). Prussian blue staining further validated the presence of intracellular cytoplasmic iron inside the tumor, which was attributed to magnetic particles adjacent to the tumors in AML-treated mice. The tumor TUNEL assay result shown in Figure 6b assuredly showed that the tumors exhibited extensive cavitation regions and high populations of apoptotic cells (brown cell) for AMLs in the magnetic field group. According to statistics, AMLs in the magnetic field treatment group exhibited higher apoptosis rates ($21.5 \pm 7.4\%$) than AMLs without magnetic field treatment ($15.4 \pm 4.5\%$). Furthermore, much more substantial tissue cavitation and necrotic cell portions were observed for AMLs than ALs in tumor suppression and necrosis (Figure S5, Supporting Information). This can be attributed to the potentially higher amount of H_2S bubbles generated from AMLs compared to ALs because of magnetic guidance. The enhanced AMLs in the tumor are beneficial for a number of gas bubbles gathered in the tumor site, which could be critical for US imaging and treatment.[40] The intratumoral bubbles bombed in the tumor can cause necrotic cell death and suppressed tumor growth more prominently compared to the AL group. As one of the gasotransmitters, the H_2S molecules after disruption could rapidly travel through deep tumor membrane barriers, resulting in an enhanced antitumor effect. The high intratumoral levels of H_2S may further facilitate tumor metastasis. In addition, there are no noticeable mortality and body weight discrepancies (Figure S6a, Supporting Information) among blank liposomes, ALs, and AMLs with and without magnetic field exposure, indicating a well-tolerated dose level and the biosafety of the AMLs. The evolution of tumor growth after 7-day follow-up observation is presented in Figure S6b (Supporting Information). AMLs with magnetic field treatment exhibited extremely significantly higher inhibitions of tumor growth than other groups, which suggested that magnetically induced AML accumulation and high intratumoral concentration of H_2S production can greatly enhance tumor growth inhibition effects.

CONCLUSIONS

In summary, AMLs are elaborately fabricated as smart liposomes to enhance the localization and efficacy of therapeutic payloads with highly spatially and temporally controlled pharmacokinetics due to the EPR and external magnetic targeting. Importantly, with the release of ADT molecules within the tumor microenvironment, *in situ* H_2S bubbles can be continually produced from AMLs, which respond to low acoustic intensity for US imaging and to high acoustic intensity for US therapy. Thus, the presence of ADT doped in the lipid shell of AMLs has transformed conventional nanoliposomes from a unimodal MR contrast agent and delivery carrier to a dual modality contrast agent in which the resultant H_2S bubbles have both imaging and therapeutic properties. The generated H_2S bubbles can bomb the cancer tissue with accurate US real-time image guidance. This proposed strategy with both enhanced tumor accumulations of nanocarriers and smart nanosize to microsize conversion properties holds great promise for overcoming tumor recurrence and treatment escape based on the accurate "treat with the eyes" medical paradigm.

DOI: 10.1021/acsnano.6b06815
ACS Nano 2017, 11, 1509–1519

Our research confirmed that the AMLs are feasible as both synergistic agents to strengthen tumor ablation efficiency and dual-mode contrast agents to provide significant contrast enhancement for MR and ultrasound imaging. However, further in-depth exploration of the physicochemical and physiological processes that AMLs are subjected to within tumor microenvironments needs to be addressed. Careful studies need to be done on investigating and improving the safety profile of H_2S bubble production systems. The long-term tumor ablation effect, cure, and survival rates as well as the biocompatibility of AMLs should be recognized before extensive applications in the clinic. The continuing studies of AMLs may lead to the development of a theranostics paradigm.

MATERIALS AND METHODS

Materials. 1,2-Dipalmitoyl-*sn*-glycero-3-phosphocholine (DPPC), 1,2-distearoyl-*sn*-glycero-3-phosphocholine (DSPC), and 1,2-distearoyl-*sn*-glycero-3-phosphoethanolamine-*N*-[(carboxyl(polyethylene glycol) 2000] (ammonium salt) (DSPE-PEG2K) lipids were purchased from Avanti Polar Lipids Inc. (Alabaster, AL, USA). 5-(4-Methoxyphenyl)-1,2-dithiole-3-thione (ADT, $C_{10}H_8OS_3$, M_w = 240.35) was provided by China Pharmaceutical University Center of Drug Discovery. γ-Fe_2O_3 superparamagnetic iron oxide nanoparticles (MNPs, mean TEM diameter: 7 nm, mean hydrodynamic diameter: 30 nm) were provided by the Jiangsu Key Laboratory for Biomaterials and Devices (China).[31] DiR (1,1′-dioctadecyl-3,3,3′,3′-tetramethylindotricarbocyanine iodide), cell membrane fluorescent dye, was purchased from KeyGEN BioTech (Nanjing, China). All other chemicals were were used as received.

AML Fabrication and Characterization. AMLs were prepared by a hydration and membrane-filtering method. Chloroform solutions of DPPC, DSPC, DSPE-PEG2K, and ADT were prepared. After an appropriate amount of DPPC, DSPC, and DSPE-PEG2K (90:5:5, molar ratio) was fully dissolved in chloroform, ADT (0.15 mg) was added to the mixture solution. Chloroform was then removed under N_2 followed by evaporation under a vacuum for at least 2 h. PBS (pH = 7.4 ± 0.1, 5 mL) with γ-Fe_2O_3 superparamagnetic iron oxide nanoparticles (250 μL, 4.0 mg/mL) was added to the dried lipids to create a lipid concentration of 20.4 μM (6.0 mg/mL). The lipid suspension was mixed well above the phase transition temperature of the lipids (60 °C) to form a milky solution of multilamellar vesicles. The solution was then extruded through a liposome extruder (T001, ATS Engineering Inc., Canada) with a polycarbonate membrane with a pore diameter of 200 nm above the phase transition temperature of the lipid mixture. Nonencapsulated MNPs and ADT were removed by passing the extruded liposomal suspension through a Sephadex G-50 spin column (15 × 1 cm, GE Healthcare, Biosciences, Piscataway, NJ, USA) equilibrated with saline (0.9% sodium chloride). The pure ADT- and MNP-loaded liposomes were collected after eluting with phosphate buffer (pH = 6.5) with a flow rate of 1 mL/min at room temperature. The final pressurized liposome solutions were stable at 4 °C. The control liposomes were prepared using the same method just without adding ADT or MNPs. In order to study the biodistribution of AMLs in tumor-bearing mice, the AMLs were labeled by the cell membrane red fluorescent dye DiR.

The size and size distribution were measured using a NanoSizer (Zeta-Sizer, Malvern Instrument, British) at a 90° scattering angle. The morphology of the liposomes was characterized by TEM (JEOL 100 CX, Japan). The magnetization properties of the samples were studied using a VSM (model 7407, Lake Shore Cryotronics, Inc., USA). The samples included liposomes, ALs, and AMLs. All the samples were tested in dry powder form.

Quantification of ADT and MNP Concentration in Liposomes. In order to quantitatively measure the concentration of ADT and MNPs loaded in the AMLs, first the AMLs were disintegrated using Triton X-100 in 30 mM EDTA. A UV−vis spectrophotometer (UV-3600, Shimadzu, Japan) was employed to quantify the ADT concentration at a wavelength of 432 nm. The MNP concentration was determined by using the 1,10-phenanthroline spectrophotometric method at a wavelength of 510 nm.

The magnetic resonance imaging (MRI) of the AML solution *in vitro* was performed using a PharmaScan 7.0 T system (BioSpin MRI GmbH Bruker, Germany). The sample was placed in an Eppendorf tube of 1 cm in diameter. At the beginning of each measurement, automatic shimming and preparation scans were performed with deionized water. The imaging parameters for T_2* (spin−spin interaction relaxation time constant)-weighted fast spin−echo were set as repetition time (TR) = 2000 ms, echo time (TE) = 30 ms, number of average = 4, echo train length = 8, and flip angle = 180°. Images were obtained with a matrix size of 256 × 256, slice thickness of 1 mm, and field of view of 40 mm × 40 mm. We continuously measured the resulting change in the transverse relaxation time (T_2*) of the sample suspension by recording the above-mentioned single-slice gradient-echo signal. No phase or frequency encoding was used. The results were analyzed by ParaVision 5.0 software. According to the monoexponential signal decay as a function of TE, the transverse relaxation time (T_2*) of the well-mixed sample suspension can be estimated.

Real-Time Visualization, Quantification of Intracellular H_2S Bubble Generation, and Cell Apoptosis. HepG2 cells (human hepatocellular carcinoma) and L02 cells (normal hepatocytes) were purchased from the Institute of Biochemistry and Cell Biology, Shanghai Institute of Biological Sciences, Chinese Academy of Sciences. The cells were cultured in RPMI 1640 medium containing 10% fetal calf serum, penicillin (100 μg/mL), and streptomycin (100 μg/mL). The cells were incubated at 37 °C in a 5% CO_2 humidified atmosphere, and medium was replaced every other day. Exponentially growing cells were harvested and were plated at the amount of 1×10^6 cells per well in six-well plates (Greiner Bio-One, USA) to allow attachment and growth overnight for cellular uptake experiments. Nanoconstructs including liposomes (100 μL), ALs (100 μL, 14.7 μg/mL ADT), and AMLs (100 μL, 14.7 μg/mL ADT, 172.1 μg/mL MNPs) were added to the wells. The H_2S bubble generation from samples was monitored in real time at room temperature using an optical microscope (IX71, Olympus Co. Ltd., Japan) equipped with a 40× focal oil lens within 24 h, which is shown in Figure 3a. Meanwhile, the amount of H_2S generated from cells was measured using a multichannel gas detector (IQ-1000, International Sensor Technology) with a H_2S gas sensor (International Sensor Technology) of a quadrupole mass spectrometer (Prisma QME 200, Germany) equipped with a Faraday cup detector.

Cell viability was measured by the CCK-8 assay (Cell Counting Kit-8, KeyGen, China) method according to the manufacturer's instructions. In order to understand whether the cell viability of ALs and AMLs is dependent on co-incubation time and ADT concentration, cell viability was measured after co-incubation for different time frames (0, 0.5, 1, 2, 4, 8, 12, and 24 h) and different ADT concentrations (1.49, 2.98, and 5.96 μg/mL). After incubation, cells were washed twice with PBS, and CCK-8 reagent was added to each well and co-incubated with cells for 1.5 h at 37 °C. The ODs of each well at 450 nm (for soluble dye) and 650 nm (for viable cells) were detected.

Moreover, the cytotoxicity of blank liposomes, ALs, and AMLs with the highest ADT concentrations (5.96 μg/mL) to L02 cells was also evaluated after co-incubation at 0, 0.5, 1, 2, 4, 8, 12, and 24 h by the CCK-8 assay.

***In Vivo* US/MRI Tumor Imaging.** All animal treatments and surgical procedures followed the approved protocols and were performed in compliance with guidelines set by the Animal Research Ethics Board of Southeast University. The female BALB/c nude mice with HepG2 xenograft tumor aged 8−10 weeks (about 20 g, 100 mm^3 tumor size) were obtained from Nanjing Source Biotechnology Co. Ltd., Nanjing, China. All mice were randomly divided into three groups (n = 5 per group): group 1, mice injected with blank liposomes; group 2, mice injected with ALs; and group 3, mice injected with AMLs. During the injection, the intact magnetic field was fixed around the tumor region and exposed for 2 h.

DOI: 10.1021/acsnano.6b06815
ACS Nano 2017, 11, 1509−1519

Before US imaging, mice were anesthetized by inhalation of 2% isoflurane with 1% oxygen. A PBS solution (200 μL, pH 7.4) containing AMLs (10 mg/mL, 10 mg/kg of drug 0.33 mg equivalent) was administered by tail vein injection. The tumor was imaged with a high-resolution microimaging system (VisualSonics Vevo 2100, Canada) with the transducer at 18 MHz of a static state using both B-mode and contrast mode. The imaging settings for the ultrasound imaging system are center frequency of 18 MHz, intensity power of 4%, and contrast gain of 35 dB. A grayscale mapping function was used to calibrate the ultrasound video intensity to ensure the video-image results were in the linear region. The mean video intensity in the regions of interest (ROIs) of the tumor was analyzed and normalized to the video intensity at the time of contrast agent injection (time = 0). In the control experiments, the same volume of blank liposomes and ALs was injected in the same way, and the tumor US images were obtained. Time-dependent US imaging was monitored at different time points (0, 2, 4, 6, 8, 12, and 24 h) after sample injection. For normalized US signals, US intensity of the background was subtracted from the intensity from AMLs injected in the tumor region and then divided by US intensity of the background.

The *in vivo* MRI experiments were performed under the same experimental conditions with the use of a 3.8 cm circular surface coil in transmit/receive mode, conducted on a PharmaScan 7.0 T system (BioSpin MRI GmbH Bruker, Germany). The mice were anesthetized with isoflurane (1.5 vol %) *via* a nose cone. Body temperature was maintained at 37 °C. The samples were then injected through the tail vein of the mice. A two-dimensional T_2* fast low-angle shot sequence with respiratory gating control was employed. The parameters for T_2* were set as repetition time (TR) = 421 ms, echo time (TE) = 5 ms, number of average = 4, echo train length = 1, flip angle = 30°. Images were obtained with a matrix size of 512 × 512, slice thickness of 1 mm, and field of view of 40 mm × 40 mm. The signal intensity was measured in ROIs in the tumor area. The total imaging observation time was 0, 2, 4, 6, 8, 12, and 24 h for each mouse.

AML Biodistribution Measurement by NIR-Fluorescence Imaging. In order to evaluate the distribution after AML injection to the HepG 2-bearing mice, NIR fluorescence *in vivo* imaging (IVIS Spectrum, Caliper Life Science, USA) was carried out. The instrument was used to record the NIR emission spectra of DiR-labeled AMLs within live mice under the conditions with and without magnetic field treatment or from their excised organs. The captured images were analyzed by Living Image 5.0 software.

***In Vivo* Tumor Therapeutic Strategy.** Using ultrasound guidance, the above-mentioned mice were treated by high acoustic intensity. For the intratumoral bubble cavitation studies, we used the following parameters: center frequency of 18 MHz, power intensity of 100%, and gain of 35 dB. In addition, the mice were weighed by electronic balance and their tumor growth was measured by vernier calipers on an alternate day. The tumor volumes were calculated as $V = d^2 \times D/2$ (where d and D represent the shortest and longest diameter of the tumor in millimeters, respectively). The total therapeutic observation lasted for 7 days.

Histology. Mice were sacrificed by cervical vertebra dislocation at 24 h postinjection after imaging and therapy. Subsequently, tumors in each group were immediately excised and weighed, followed by fixing in 10% formalin. After being embedded in paraffin, ultrathin sections (50 nm) were obtained. The nuclear fast red for the cell nucleus and Prussian blue dye for magnetic nanoparticles were successively used for staining. In order to further evaluate the apoptotic response in tumor tissue, we used the commercially available colorimetric TdT-mediated dUTP nick-end labeling (TUNEL) apoptosis assay kits (Beyotime Institute of Biotechnology, China) for tumor sections according to the manufacturer's instructions. Five equal-sized fields were randomly chosen to observe by optical microscopy.

Statistical Analysis. The normal data are expressed as mean ± standard deviation with a sample size of 3 and were carried out using SPSS 13.0 software (Chicago, IL, USA). Comparisons were conducted using one-way analysis of variance (ANOVA) followed by a Student's t test. Values of $^*p < 0.05$ and $^{**}p < 0.01$ were considered statistically significant. All reported p values are two-tailed.

ASSOCIATED CONTENT

Supporting Information

The Supporting Information is available free of charge on the ACS Publications website at DOI: 10.1021/acsnano.6b06815.

Measurement of iron concentration in AMLs, Prussian blue staining for HepG2 cell uptake of AMLs, HepG2 cell viability when incubated with AMLs of different ADT concentrations as well as L02 cell viability when incubated with AMLs, schematic of *in vivo* US/MRI imaging and therapy setup and the standardized protocols, HE and Prussian blue staining for blank liposome- and AL-treated groups, body weight change and tumor volume change of a 7-day follow-up experiment (PDF)

Optical microscopic dynamics acquisition of the H_2S microbubble production process in *in situ* HepG2 cells (AVI)

AUTHOR INFORMATION

Corresponding Authors

*E-mail (F. Yang): yangfang2080@seu.edu.cn.
*E-mail (N. Gu): guning@seu.edu.cn.

ORCID

Ning Gu: 0000-0003-0047-337X

Author Contributions

§Y. Liu and F. Yang contributed equally to this work.

Notes

The authors declare no competing financial interest.

ACKNOWLEDGMENTS

This investigation was financially funded by a project of National Key Basic Research Program of China (2013CB733804) and National Natural Science Foundation of China (31370019, 61420106012). The funding partially also comes from the Author of National Excellent Doctoral Dissertation of China (No. 201259), as well as the Fundamental Research Funds for the Central Universities and Zhong Ying Young Scholar of Southeast University. The authors also would like to thank the Collaborative Innovation Center of Suzhou Nano Science and Technology for support. We appreciate Prof. Hai Qian of China Pharmaceutical University for providing anethole dithiolethione and valuable discussions. We are also thankful to Dr. Fengchao Zang and Prof. Gaojun Teng from Jiangsu Key Laboratory of Molecular and Functional Imaging for the mouse magnetic resonance imaging experiment.

REFERENCES

(1) Mura, S.; Nicolas, J.; Couvreur, P. Stimuli-Responsive Nanocarriers for Drug Delivery. *Nat. Mater.* **2013**, *12*, 991−1003.

(2) Barreto, J. A.; O'Malley, W.; Kubeil, M.; Graham, B.; Stephan, H.; Spiccia, L. Nanomaterials: Applications in Cancer Imaging and Therapy. *Adv. Mater.* **2011**, *23*, H18−40.

(3) Zhang, Y.; Yu, J.; Bomba, H. N.; Zhu, Y.; Gu, Z. Mechanical Force-Triggered Drug Delivery. *Chem. Rev.* **2016**, *116*, 12536−12563.

(4) Wang, S.; Wang, H.; Liu, Z.; Wang, L.; Wang, X.; Su, L.; Chang, J. Smart pH- and Reduction-Dual-Responsive Folate-PEG-Coated Polymeric Lipid Vesicles for Tumor-Triggered Targeted Drug Delivery. *Nanoscale* **2014**, *6*, 7635−7642.

(5) Ko, H.; Son, S.; Jeon, J.; Thambi, T.; Kwon, S.; Chae, Y. S.; Kang, Y. M.; Park, J. H. Tumor Microenvironment-Specific Nanoparticles

Activatable by Stepwise Transformation. *J. Controlled Release* **2016**, *234*, 68−78.
(6) Brigger, I.; Dubernet, C.; Couvreur, P. Nanoparticles in Cancer Therapy and Diagnosis. *Adv. Drug Delivery Rev.* **2002**, *54*, 631−651.
(7) Xie, J.; Zhang, Y.; Yan, C.; Song, L.; Wen, S.; Zang, F.; Chen, G.; Ding, Q.; Yan, C.; Gu, N. High-Performance PEGylated Mn-Zn Ferrite Nanocrystals as a Passive-Targeted Agent for Magnetically Induced Cancer Theranostics. *Biomaterials* **2014**, *35*, 9126−9136.
(8) Fan, Z.; Shelton, M.; Singh, A. K.; Senapati, D.; Khan, S. A.; Ray, P. C. Multifunctional Plasmonic Shell-Magnetic Core Nanoparticles for Targeted Diagnostics, Isolation, and Photothermal Destruction of Tumor Cells. *ACS Nano* **2012**, *6*, 1065−1073.
(9) Spring, B. Q.; Bryan Sears, R.; Zheng, L. Z.; Mai, Z.; Watanabe, R.; Sherwood, M. E.; Schoenfeld, D. A.; Pogue, B. W.; Pereira, S. P.; Villa, E.; Hasan, T. A Photoactivable Multi-Inhibitor Nanoliposome for Tumour Control and Simultaneous Inhibition of Treatment Escape Pathways. *Nat. Nanotechnol.* **2016**, *11*, 378−387.
(10) Wang, Y.; Shim, M. S.; Levinson, N. S.; Sung, H. W.; Xia, Y. Stimuli-Responsive Materials for Controlled Release of Theranostic Agents. *Adv. Funct. Mater.* **2014**, *24*, 4206−4220.
(11) Allen, T. M.; Cullis, P. R. Liposomal Drug Delivery Systems: From Concept to Clinical Applications. *Adv. Drug Delivery Rev.* **2013**, *65*, 36−48.
(12) Chen, G.; Wang, L.; Cordie, T.; Vokoun, C.; Eliceiri, K. W.; Gong, S. Multi-Functional Self-Fluorescent Unimolecular Micelles for Tumor-Targeted Drug Delivery and Bioimaging. *Biomaterials* **2015**, *47*, 41−50.
(13) Howes, P. D.; Chandrawati, R.; Stevens, M. M. Colloidal Nanoparticles as Advanced Biological Sensors. *Science* **2014**, *346*, 1247390.
(14) Jing, L.; Ding, K.; Kershaw, S. V.; Kempson, I. M.; Rogach, A. L.; Gao, M. Magnetically Engineered Semiconductor Quantum Dots as Multimodal Imaging Probes. *Adv. Mater.* **2014**, *26*, 6367−6386.
(15) Blanco, E.; Shen, H.; Ferrari, M. Principles of Nanoparticle Design for Overcoming Biological Barriers to Drug Delivery. *Nat. Biotechnol.* **2015**, *33*, 941−951.
(16) Durymanov, M. O.; Rosenkranz, A. A.; Sobolev, A. S. Current Approaches for Improving Intratumoral Accumulation and Distribution of Nanomedicines. *Theranostics* **2015**, *5*, 1007−1020.
(17) Raeesi, V.; Chan, W. C. Improving Nanoparticle Diffusion Through Tumor Collagen Matrix by Photo-Thermal Gold Nanorod. *Nanoscale* **2016**, *8*, 12524−12530.
(18) Holback, H.; Yeo, Y. Intratumoral Drug Delivery with Nanoparticulate Carriers. *Pharm. Res.* **2011**, *28*, 1819−1830.
(19) Paoli, E. E.; Ingham, E. S.; Zhang, H.; Mahakian, L. M.; Fite, B. Z.; Gagnon, M. K.; Tam, S.; Kheirolomoom, A.; Cardiff, R. D.; Ferrara, K. W. Accumulation, Internalization and Therapeutic Efficacy of Neuropilin-1-Targeted Liposomes. *J. Controlled Release* **2014**, *178*, 108−117.
(20) Valencia, P. M.; Hanewich-Hollatz, M. H.; Gao, W.; Karim, F.; Langer, R.; Karnik, R.; Farokhzad, O. C. Effects of Ligands with Different Water Solubilities on Self-Assembly and Properties of Targeted Nanoparticles. *Biomaterials* **2011**, *32*, 6226−6233.
(21) Chen, F.; Hong, H.; Goel, S.; Graves, S. A.; Orbay, H.; Ehlerding, E. B.; Shi, S.; Theuer, C. P.; Nickles, R. J.; Cai, W. *In Vivo* Tumor Vasculature Targeting of CuS@MSN Based Theranostic Nanomedicine. *ACS Nano* **2015**, *9*, 3926−3934.
(22) Wang, J.; Tian, S.; Petros, R. A.; Napier, M. E.; DeSimone, J. M. The Complex Role of Multivalency in Nanoparticles Targeting the Transferrin Receptor for Cancer Therapies. *J. Am. Chem. Soc.* **2010**, *132*, 11306−11313.
(23) Lazarovits, J.; Chen, Y. Y.; Sykes, E. A.; Chan, W. C. W. Nanoparticle-Blood Interactions: the Implications on Solid Tumour Targeting. *Chem. Commun.* **2015**, *51*, 2756−2767.
(24) Au, J. L.; Yeung, B. Z.; Wientjes, M. G.; Lu, Z.; Wientjes, M. G. Delivery of Cancer Therapeutics to Extracellular and Intracellular Targets: Determinants, Barriers, Challenges and Opportunities. *Adv. Drug Delivery Rev.* **2016**, *97*, 280−301.
(25) Huang, J.; Li, Y.; Orza, A.; Lu, Q.; Guo, P.; Wang, L.; Yang, L.; Mao, H. Magnetic Nanoparticle Facilitated Drug Delivery for Cancer Therapy with Targeted and Image-Guided Approaches. *Adv. Funct. Mater.* **2016**, *26*, 3818−3836.
(26) Prabhakar, U.; Maeda, H.; Jain, R. K.; Sevick-Muraca, E. M.; Zamboni, W.; Farokhzad, O. C.; Barry, S. T.; Gabizon, A.; Grodzinski, P.; Blakey, D. C. Challenges and Key Considerations of the Enhanced Permeability and Retention Effect for Nanomedicine Drug Delivery in Oncology. *Cancer Res.* **2013**, *73*, 2412−2417.
(27) Fiorucci, S.; Orlandi, S.; Mencarelli, A.; Caliendo, G.; Santagada, V.; Distrutti, E.; Santucci, L.; Cirino, G.; Wallace, J. L. Enhanced Activity of a Hydrogen Sulphide-Releasing Derivative of Mesalamine (ATB-429) in a Mouse Model of Colitis. *Br. J. Pharmacol.* **2007**, *150*, 996−1002.
(28) Predmore, B. L.; Lefer, D. J.; Gojon, G. Hydrogen Sulfide in Biochemistry and Medicine. *Antioxid. Redox Signaling* **2012**, *17*, 119−140.
(29) Kiessling, F.; Fokong, S.; Bzyl, J.; Lederle, W.; Palmowski, M.; Lammers, T. Recent Advances in Molecular, Multimodal and Theranostic Ultrasound Imaging. *Adv. Drug Delivery Rev.* **2014**, *72*, 15−27.
(30) Szabo, C. Gasotransmitters in Cancer: From Pathophysiology to Experimental Therapy. *Nat. Rev. Drug Discovery* **2016**, *15*, 185−203.
(31) Chen, B.; Li, Y.; Zhang, X.; Liu, F.; Liu, Y.; Xiong, F.; Gu, N. An Efficient Synthesis of Ferumoxytol Induced by Alternating-Current Magnetic Field. *Mater. Lett.* **2016**, *170*, 93−96.
(32) Kashfi, K.; Olson, K. R. Biology and Therapeutic Potential of Hydrogen Sulfide and Hydrogen Sulfide-Releasing Chimeras. *Biochem. Pharmacol.* **2013**, *85*, 689−703.
(33) Wu, D.; Si, W.; Wang, M.; Lv, S.; Ji, A.; Li, Y. Hydrogen Sulfide in Cancer: Friend or Foe? *Nitric Oxide* **2015**, *50*, 38−45.
(34) Hellmich, M. R.; Coletta, C.; Chao, C.; Szabo, C. The Therapeutic Potential of Cystathionine Beta-Synthetase/Hydrogen Sulfide Inhibition in Cancer. *Antioxid. Redox Signaling* **2015**, *22*, 424−448.
(35) Budde, M. W.; Roth, M. B. Hydrogen Sulfide Increases Hypoxia-Inducible Factor-1 Activity Independently of Von Hippel-Lindau Tumor Suppressor-1 in C. elegans. *Mol. Biol. Cell* **2010**, *21*, 212−217.
(36) De Preter, G.; Deriemaeker, C.; Danhier, P.; Brisson, L.; Pham, T. T. C.; Grégoire, V.; Jordan, B. F.; Sonveaux, P.; Gallez, B. A Fast Hydrogen Sulfide-Releasing Donor Increases the Tumor Response to Radiotherapy. *Mol. Cancer Ther.* **2016**, *15*, 154−161.
(37) Theek, B.; Baues, M.; Ojha, T.; Möckel, D.; Veettil, S. K.; Steitz, J.; van Bloois, L.; Storm, G.; Kiessling, F.; Lammers, T. Sonoporation Enhances Liposome Accumulation and Penetration in Tumors with Low EPR. *J. Controlled Release* **2016**, *231*, 77−85.
(38) Bertrand, N.; Wu, J.; Xu, X.; Kamaly, N.; Farokhzad, O. C. Cancer Nanotechnology: the Impact of Passive and Active Targeting in the Era of Modern Cancer Biology. *Adv. Drug Delivery Rev.* **2014**, *66*, 2−25.
(39) Xing, H.; Hwang, K.; Lu, Y. Recent Developments of Liposomes as Nanocarriers for Theranostic Applications. *Theranostics* **2016**, *6*, 1336−1352.
(40) Chertok, B.; Langer, R.; Anderson, D. G. Spatial Control of Gene Expression by Nanocarriers Using Heparin Masking and Ultrasound-Targeted Microbubble Destruction. *ACS Nano* **2016**, *10*, 7267−7278.

DOI: 10.1021/acsnano.6b06815
ACS Nano 2017, 11, 1509−1519